RESEARCH ARTICLE

ADVANCED MATERIALS INTERFACES Open Access

www.advmatinterfaces.de

Tunable Photoluminescence from Monolayer Molybdenum Disulfide

Brendan F. M. Healy, Sophie L. Pain, James Lloyd-Hughes, Nicholas E. Grant, and John D. Murphy**

Monolayer molybdenum disulfide (1L MoS_2), a promising optoelectronic material, emits strong visible photoluminescence (PL). Systematic control of the intensity, energy, and spectral width of PL from 1L MoS_2 on silicon dioxide/silicon (SiO_2/Si) is demonstrated via simple external treatments. Treating MoS_2 with solutions formed from the superacid bis-(trifluoromethanesulfonyl)amide (TFSA) enhances, blueshifts, and sharpens the PL. Treatments with solutions from structurally analogous chemicals that lack sulfur, in the case of bis(trifluoroacetamide) (BTFA), or lack fluorine, in the case of methanesulfonamide (MSA), show the same trend, suggesting a two-component mechanism for TFSA involving the presence of electronegative species and sulfur vacancy passivation. Up to ≈100× enhancement of the PL intensity is achieved, with the peak blueshifted by ≈30 meV and the spectral linewidth halved. Conversely, direct thermal atomic layer deposition (ALD) of aluminum oxide (Al_2O_3) or hafnium oxide (HfO_2) is found to suppress the PL by up to a factor of ≈3, redshift by up to ≈70 meV, and broaden by ≈3×. Single-spot and mapping Raman/PL techniques are combined in a robust characterization process to associate changes in the PL character to charge doping. This work demonstrates the convenient tunability of the optical behavior of 1L MoS_2 by varying the electron density.

1. Introduction

Transition metal dichalcogenides (TMDCs) are an exciting class of 2D materials that exhibit exceptional physical and chemical behavior at monolayer thickness.[1,2] Molybdenum disulfide (MoS_2), a prototypical TMDC, is a leading candidate for inclusion in numerous optoelectronic technologies, owing to its novel optical properties.[3–7] Monolayer MoS_2 (1L MoS_2) comprises a hexagonal plane of Mo atoms sandwiched between two hexagonally arranged planes of S atoms to yield a S-Mo-S structure with a thickness of ≈0.7 nm.[3,8–11] With a direct bandgap in the visible spectral range, 1L MoS_2 emits a relatively strong photoluminescence (PL) signal.[9]

The ability to control the PL character of MoS_2 is necessary for the full realization of its optoelectronic potential. The 1L MoS_2 PL spectrum is sensitive to a range of external treatments,[12] including oxygen plasma exposure,[13] annealing,[14,15] laser irradiation,[16,17] interaction with plasmonic metal nanoparticles,[18–21] superacid chemical treatment,[22] and dielectric encapsulation.[23] Each treatment induces a specific response in the intensity, energy and spectral width of the PL emission from 1L MoS_2. Although responsive to numerous treatments, the PL properties of synthesized MoS_2 films depend strongly on the growth process and target substrate, including post-synthesis transfer to alternative substrates,[24–26] hence drawing reliable conclusions from a broad range of different studies can be challenging. In this study, we focus on 1L MoS_2 films grown on silicon dioxide/silicon (SiO_2/Si) via chemical vapor deposition (CVD).

Here, we develop processes that enable the PL emission from 1L MoS_2 to be controlled reliably, with a focus on chemical treatments and direct thermal atomic layer deposition (ALD) of dielectrics. Prior work has shown that exposing 1L MoS_2 to a solution containing superacidic bis-(trifluoromethanesulfonyl)amide (often TFSI or $HNTf_2$ but herein TFSA) substantially enhances absolute PL intensity, with accompanying upwards energy shift and narrowing of the PL signal also commonly seen.[22,27,28] On the other hand, thermal ALD of a high dielectric constant (high-κ) material, commonly aluminum oxide (Al_2O_3) or hafnium oxide (HfO_2), on MoS_2 has been shown to deplete, redshift and broaden the PL signal.[23,29–32] In this work, we present a novel comparison of the influence of chemical submersion and ALD of high-κ materials on the PL character of CVD-grown 1L MoS_2 films. We also treat 1L MoS_2 with chemicals structurally related to TFSA

B. F. M. Healy, S. L. Pain, N. E. Grant, J. D. Murphy
School of Engineering
University of Warwick
Coventry CV4 7AL, UK
E-mail: brendan.healy@warwick.ac.uk; john.d.murphy@warwick.ac.uk

J. Lloyd-Hughes
Department of Physics
University of Warwick
Coventry CV4 7AL, UK

The ORCID identification number(s) for the author(s) of this article can be found under https://doi.org/10.1002/admi.202400305

© 2024 The Author(s). Advanced Materials Interfaces published by Wiley-VCH GmbH. This is an open access article under the terms of the Creative Commons Attribution License, which permits use, distribution and reproduction in any medium, provided the original work is properly cited.

DOI: 10.1002/admi.202400305

21967350, 2024, 28, Downloaded from https://onlinelibrary.wiley.com/doi/10.1002/admi.202400305 by Test, Wiley Online Library on [03/10/2024]. See the Terms and Conditions (https://onlinelibrary.wiley.com/terms-and-conditions) on Wiley Online Library for rules of use; OA articles are governed by the applicable Creative Commons License

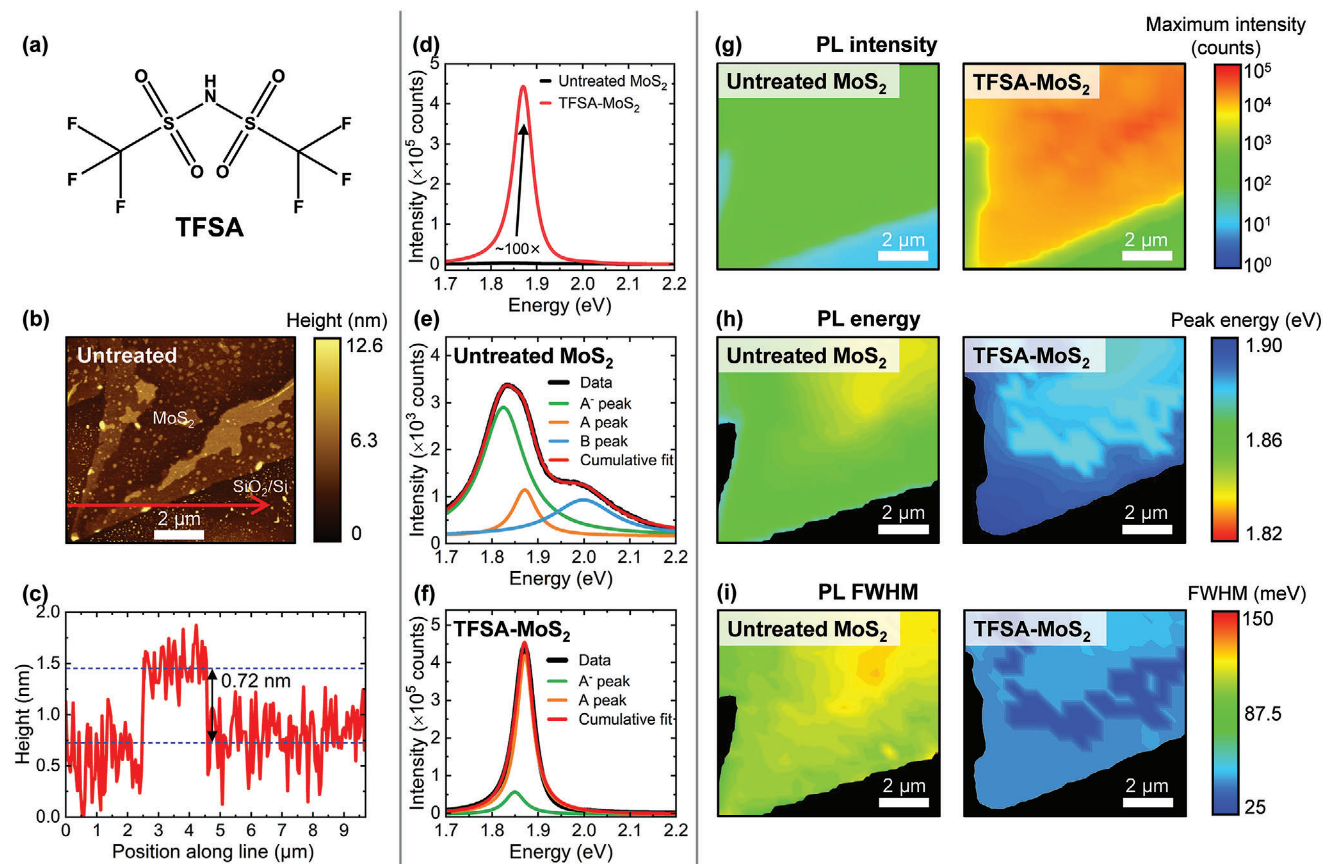

Figure 1. a) Schematic chemical structure of TFSA. b) Topographic AFM image of MoS_2 triangular structure from which PL characterization was performed. c) Height profile measured along the red arrow in (b). d) Raw single-spot PL spectra measured from 1L MoS_2 before and after submersion in a TFSA-DCM solution for 10 min. Multipeak deconvolution of the PL spectrum obtained from 1L MoS_2 e) before and f) after TFSA treatment. The cumulative fit, and contributions of the A^-, A and B peaks are given in red, green, orange, and blue, respectively. Maps of the g) maximum absolute PL intensity, h) peak PL energy, and i) FWHM of the PL signal emitted from MoS_2 before and after TFSA treatment. The logarithmic scale should be noted in (g).

to elucidate a deeper understanding of TFSA-facilitated PL enhancement. Moreover, we demonstrate that the differing effects that arise from chemical and ALD-based treatments enable selective modification of the PL behavior of 1L MoS_2.

2. Results and Discussion

2.1. Chemical Treatment

We first discuss the influence of TFSA treatment on the optical behavior of 1L MoS_2. The chemical structure of TFSA is depicted schematically in **Figure** 1a. A cleaved CVD-grown 1L MoS_2 on (SiO_2/Si) sample was submerged in a TFSA-dichloromethane (DCM) solution for 10 min, with the Raman and PL signals from a MoS_2 triangular structure close to the edge of the continuous MoS_2 film measured before and after treatment. The MoS_2 region monitored via Raman/PL spectroscopy is shown in the atomic force microscopy (AFM) image in Figure 1b, with the thickness of ≈0.7 nm extracted from the height trace in Figure 1c confirming its monolayer nature.[3,9,10] Further characterization of the CVD-grown 1L MoS_2 films used in this study is provided in Figure S1 (Supporting Information). Figure 1d,e displays single-spot and mapping PL spectra measured from 1L MoS_2 before and after submersion in TFSA. We have previously demonstrated that such commercially available 1L MoS_2 films exhibit a spatially variable PL signal.[24] To ensure any perceived effects did not result from site-to-site variation, we utilized mapping techniques to gain spatially resolved PL information that enabled the same sites to be located before and after treatment. We assessed the impact of submerging 1L MoS_2 in the DCM solvent only and found no significant change to the PL and Raman spectra (Figure S2, Supporting Information). Hence, any modification of the optical behavior of 1L MoS_2 following submersion in TFSA-DCM solution is attributed to TFSA.

From the single-spot spectra and maps of PL intensity, we find that TFSA treatment induces a maximum ≈100× enhancement of MoS_2 PL intensity (Figure 1d), in agreement with our previous report.[22] We also observe a significant blueshift (≈30 meV) in the position of the PL emission and substantial narrowing (≈80 meV) of the full width at half maximum (FWHM). The strengthening, blueshifting and narrowing is visualized intuitively in the spatially resolved maps of the PL intensity, energy, and linewidth displayed in Figure 1g–i, respectively. It should be noted that the PL energy toward the edges of the MoS_2 flake is blueshifted

 © 2024 The Author(s). Advanced Materials Interfaces published by Wiley-VCH GmbH

21967350, 2024, 28, Downloaded from https://onlinelibrary.wiley.com/doi/10.1002/admi.202400305 by Test, Wiley Online Library on [03/10/2024]. See the Terms and Conditions (https://onlinelibrary.wiley.com/terms-and-conditions) on Wiley Online Library for rules of use; OA articles are governed by the applicable Creative Commons License

relative to the interior before and after TFSA treatment, this is a well-reported effect that arises from local variations in strain.[33–35] With the FWHM of the PL peak known to be inversely proportional to the lifetimes of the excitonic and trionic states,[36] we infer that the TFSA treatment extends these lifetimes, as Amani et al. observed via time-resolved PL (TRPL) measurements.[27] An enhanced, blueshifted and sharpened PL signal is characteristic of *p*-type doped MoS_2.[14,37] Hence, we attribute the modified 1L MoS_2 PL spectrum following TFSA treatment to a depleted electron density in MoS_2. TFSA can withdraw electron density from MoS_2 via a surface charge transfer process that is thought to result from the high electronegativity of fluorine (F) atoms in TFSA.[27,28,38–40]

To explore any TFSA-induced doping effects further, we deconvolute the single-site PL spectra obtained before and after TFSA treatment into three constituent spectral contributions: A and B exciton transitions, and an A^- trion emission. The decomposed spectra are presented in Figure 1e,f. Here, we find untreated 1L MoS_2 to exhibit a dominant trion emission at ≈1.82 eV, with A and B excitonic features at ≈1.87 and ≈2.0 eV, respectively. The ratio of the absolute trion peak intensity to that of the A exciton peak, A^-/A, can reveal information regarding the charge carrier density.[41] A large A^-/A ratio (≈4) is observed here in the untreated sample, as expected.[42] The PL spectrum of the same 1L MoS_2 sample after TFSA treatment is dominated by the A excitonic emission with a much weaker trionic contribution, yielding an A^-/A ratio of ≈0.05. Hence, we infer that TFSA treatment significantly depletes the native excess of electrons in 1L MoS_2. The markedly reduced A^-/A ratio can also explain the observed PL enhancement, since trions are known to be more susceptible to decay via non-radiative pathways than neutral excitons.[38] Moreover, the energy splitting between the A and A^- peaks is reduced from ≈46 to ≈22 meV by TFSA exposure, indicating a reduction in the trion binding energy consistent with a *p*-doping effect.[41,43]

Defect passivation, in addition to *p*-type doping by electronegative F, is thought to play a key role in the TFSA-induced PL enhancement of 1L MoS_2.[27,28,38–40] Defects in monolayer TMDCs can trap excitons and prevent their radiative recombination, thus suppressing the PL signal.[40,44] McCreary et al. proposed the ratio of the B excitonic peak intensity to that of the A exciton, B/A, as an indicator of defect density in 1L MoS_2,[45] with a larger B/A value implying a higher relative density of defect states. We extract B/A ratio information from our PL peak deconvolutions in Figure 1e,f and infer the influence of TFSA treatment on the defect site density in 1L MoS_2. We note that McCreary et al. considered the MoS_2 PL spectrum as two superposed Lorentzian curves, A and B, with any trionic contribution accounted for by the A peak. Since we employ a three-peak deconvolution, we define our exciton intensity ratio here as B/(A+A^-). We find TFSA treatment quenches the B exciton emission, with a vanishingly small B peak observed following superacid immersion. This yields a significantly decreased B/(A+A^-) ratio that supports defect passivation as a key mechanism of TFSA-mediated PL enhancement of 1L MoS_2, in agreement with numerous reports, yet the precise nature of the defect states remains unclear.[46–48] A range of structural defects, including mono- and bi-sulfur (S) vacancies, impurities, dislocations, and anti-sites have been shown to exist in CVD-1L MoS_2.[49,50] Mono-S vacancies are thought to be the most abundant point defects, owing to their low formation energy.[50–52] Roy et al. combined Raman/PL spectroscopy, scanning transmission electron microscopy (STEM) and density functional theory (DFT) to suggest that the enhanced MoS_2 PL signal arises from occupation of intrinsic mono-S vacancies by S atoms in sulfonyl molecules (SO_2) dissociated from TFSA.[40] Since S vacancies are typically negatively charged,[48] their removal will also contribute to the observed *p*-type doping of 1L MoS_2.[46,47,53,54] Hence, depletion of electron density in TFSA-treated 1L MoS_2 can be considered a two-faceted effect: the combination of surface charge transfer due to highly electronegative F atoms and passivation of S vacancy states.

To explore further the mechanisms underpinning the *p*-type doping effect observed following TFSA treatment, we treated 1L MoS_2 for 10 min in a DCM solution with a F-containing but S-free acid (bistrifluoroacetamide (BTFA)) and separately with a S-containing but F-free acid (methanesulfonamide (MSA)). BTFA, a weak Lewis acid,[22] shares a similar chemical structure with TFSA yet includes carbonyl groups in place of sulfonyl groups, indicated in **Figure 2**a. MSA is also weakly Lewis acidic and is structurally analogous to one moiety of a symmetrical TFSA species but with CF_3 substituted for CH_3, as shown in Figure 2i. Regions of the two separate cleaved 1L MoS_2 samples selected for characterizing the effects of BTSA and MSA submersion are displayed in the AFM images in Figure 2b,j, respectively. Single-spot and mapping PL spectra measured before and after the BTFA and MSA treatments are also presented in Figure 2.

We find that treating 1L MoS_2 with BTFA or MSA also yields an enhanced, blueshifted, and sharpened PL spectrum. These PL changes suggest both BTFA and MSA submersion lead to *p*-type doping of the 1L MoS_2, which is further supported by a reduced A^-/A ratio following each treatment. However, the magnitudes of the enhancement, blueshift and narrowing are less significant than those induced by TFSA treatment. The enhancements associated with BTFA or MSA treatment are only ≈2× and ≈5×, respectively. In addition, the MoS_2 PL signal is blueshifted by only ≈25 meV as a result of BTFA treatment, with an even smaller blueshift (≈7 meV) observed following MSA submersion. The PL spectral width was reduced by a factor of ≈1.3 after BTFA exposure and by ≈1.5 after MSA treatment. Evaluation of the deconvoluted single-spot PL spectra in Figure 2e,f suggests the B/(A+A^-) intensity ratio is reduced from ≈0.2 to ≈0.1 by BTFA submersion. Since the B/(A+A^-) ratio can be indicative of the defect state density present in 1L MoS_2,[45] this decrease may indicate some degree of defect passivation has occurred. However, the reduction in B/(A+A^-) ratio is less dramatic than that observed following both TFSA or MSA treatment, where the B excitonic contribution was substantially reduced in both cases. This suggests that TFSA and MSA may be more effective than BTFA at repairing defective sites in 1L MoS_2 due to the presence of S. The doping effect in BTFA-treated MoS_2 may therefore be largely due to electronegative F atoms in the BTFA molecular structure.[53]

A possible explanation for the huge PL signal enhancement from TFSA-treated MoS_2 is a synergistic effect of *p*-doping by highly electronegative F atoms in TFSA and filling of S vacancy states by dissociated SO_2 molecules. The modestly enhanced MoS_2 PL intensity following BTFA treatment may be due to a surface charge transfer *p*-type doping effect, with the absence of S atoms resulting in no sizeable defect passivation. With no highly electronegative atoms present in MSA, the doping of 1L MoS_2

© 2024 The Author(s). Advanced Materials Interfaces published by Wiley-VCH GmbH

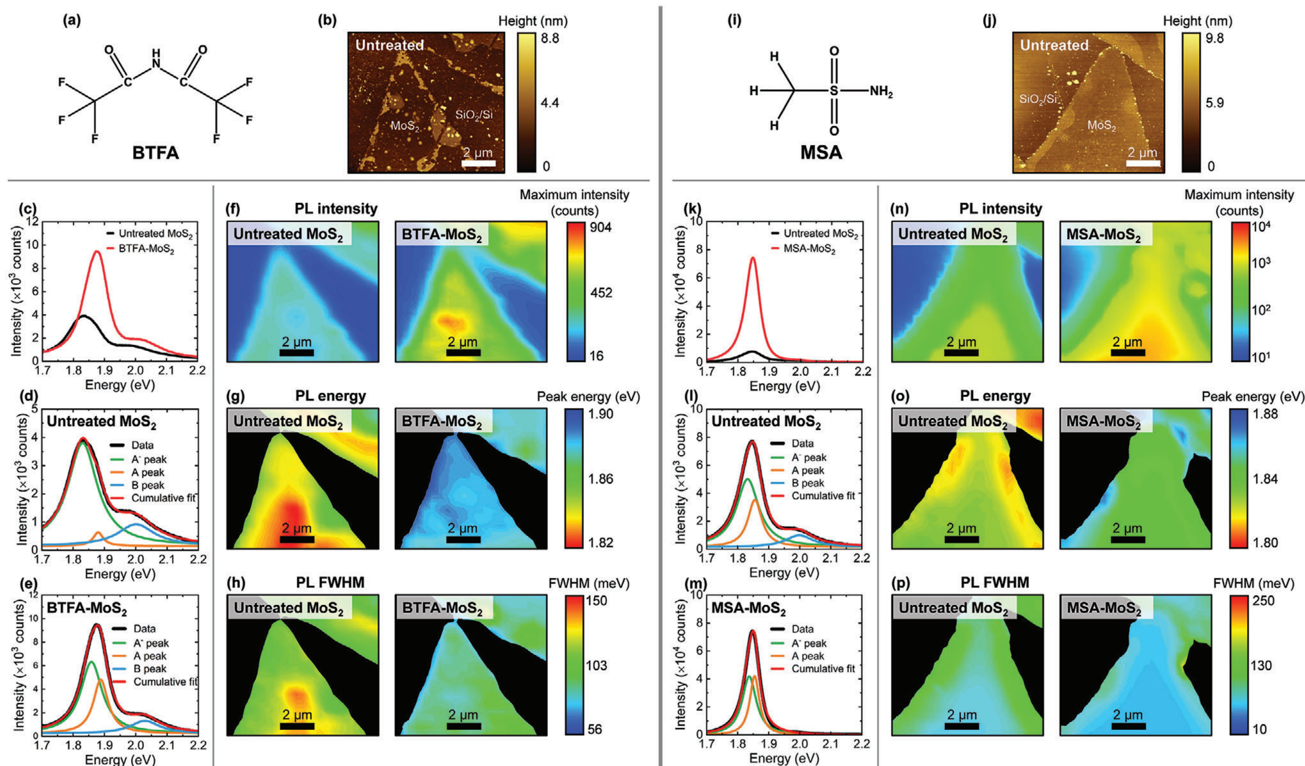

Figure 2. a) Schematic chemical structure of BTFA. b) Topographic AFM image of MoS_2 region from which BTFA-treated MoS_2 PL was characterized. c) PL spectra prior to and following BTFA treatment. Multipeak deconvolution of the obtained PL spectrum d) before and e) after BTFA treatment. Maps of f) maximum absolute PL intensity, g) peak PL energy, and h) FWHM of the PL signal emitted from the MoS_2 sample before and after BTFA treatment. i) Schematic chemical structure of MSA. j) Topographic AFM image of MoS_2 region from which MSA-treated MoS_2 PL was characterized. k) PL spectra prior to and following MSA treatment. Multipeak deconvolution of the obtained PL spectrum l) before and m) after MSA treatment. Maps of n) maximum absolute PL intensity, o) peak PL energy and p) FWHM of the PL signal emitted from the MoS_2 sample before and after MSA treatment. In (d), (e), (l), and (m), the cumulative fit, and contributions of the A^-, A and B peaks are given in red, green, orange, and blue, respectively.

by MSA treatment could result from significant removal of S vacancies.

2.2. Direct Thermal ALD of Al_2O_3 and HfO_2 on MoS_2

Next, we explore the growth of Al_2O_3 and HfO_2 films via thermal ALD on 1L MoS_2 at 200 °C. The morphology of each dielectric film was examined via AFM and **Figure 3** displays low-magnification AFM images of MoS_2 samples before and after ALD growth of Al_2O_3 and HfO_2 layers. High-magnification AFM scans of each dielectric film and approximated maps of the dielectric coverage are also presented.

Uniform film growth via ALD requires a substantial density of dangling bonds on the substrate surface to provide suitable sites for chemisorption of ALD precursors.[55] Since the basal plane of a TMDC single-layer is chemically inert, direct growth of a continuous high-κ layer on 1L MoS_2 via standard thermal ALD is challenging. Numerous studies have reported that the ALD of dielectric materials on 1L MoS_2 originates at defects sites and proceeds via physisorption of precursors, resulting in a 3D island growth mode that coalesces toward a complete layer.[30,56–59] This growth process typically results in formation of incomplete, inhomogeneous dielectric films at standard operating temperatures (e.g., 150–200 °C). Aiming for the formation of completely closed dielectric layers, we deposited a high number of ALD cycles (200 cycles) in each case. While complete surface coverage is not achieved by either Al_2O_3 or HfO_2, dense film coalescence was observed. The greatest surface coverage was seen in the HfO_2 film (≈92%), with the Al_2O_3 layer also covering a significant fraction of the underlying MoS_2 (≈85%). In both cases, the dielectric film exhibits the distinctive island morphology that has been reported elsewhere for ALD-Al_2O_3 and ALD-HfO_2 layers on MoS_2.[30,31,56,57] The average diameter of the dielectric islands was found to be larger in the Al_2O_3 film (see Figure S3, Supporting Information).

We now examine the impact of each ALD-dielectric film on the optical properties of 1L MoS_2. **Figure 4** presents single-spot PL and Raman spectra from two different cleaved 1L MoS_2 samples before and after Al_2O_3 and HfO_2 deposition. Maps of maximum PL intensity, peak PL energy, and FWHM associated with each treatment are also displayed.

Direct ALD of Al_2O_3 or HfO_2 on 1L MoS_2 was found to reduce, redshift, and broaden the PL signal, as evident in the single-spot PL spectra in Figure 4a,g. The PL mapping measurements displayed in Figure 4d–f,j–l confirm the ALD-induced changes to be prevalent across the MoS_2 surface in both cases. We have experimentally verified that no significant impact on the MoS_2 PL

© 2024 The Author(s). Advanced Materials Interfaces published by Wiley-VCH GmbH

21967350, 2024, 28, Downloaded from https://onlinelibrary.wiley.com/doi/10.1002/admi.202400305 by Test, Wiley Online Library on [03/10/2024]. See the Terms and Conditions (https://onlinelibrary.wiley.com/terms-and-conditions) on Wiley Online Library for rules of use; OA articles are governed by the applicable Creative Commons License

ADVANCED MATERIALS INTERFACES
Open Access
www.advmatinterfaces.de

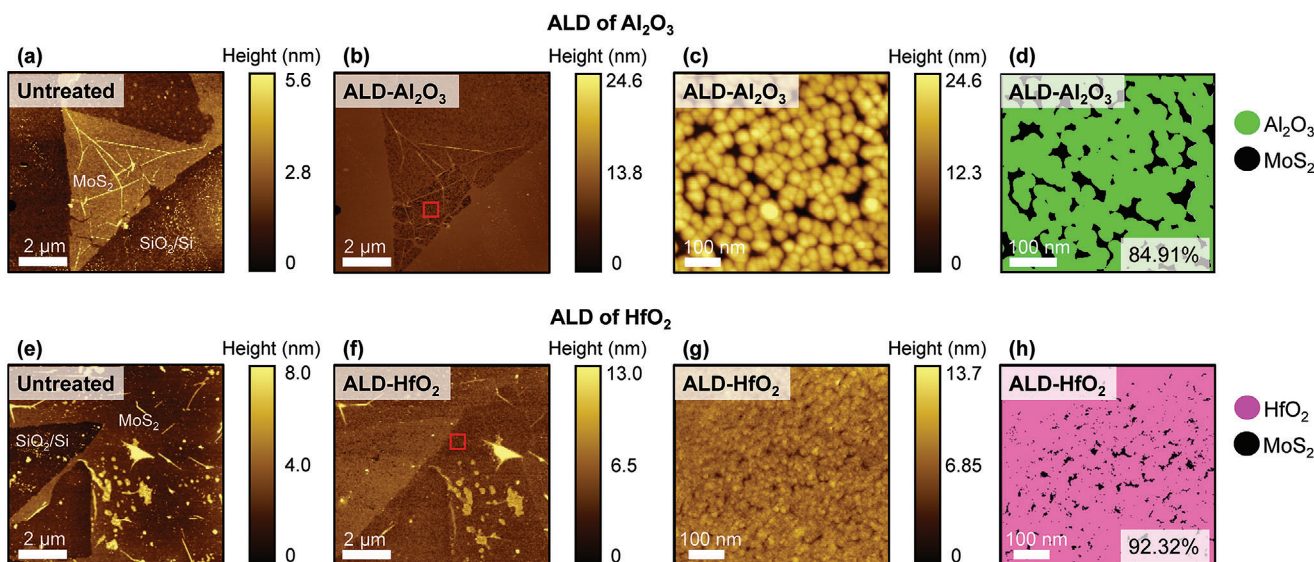

Figure 3. Low-magnification topological AFM images of 1L MoS_2 a) before and b) after ALD of Al_2O_3. c) High-magnification topological AFM images and d) estimated surface coverage of the ALD-Al_2O_3 film. The corresponding images for HfO_2 are shown in (e) to (h).

emission resulted from water exposure, thermal or vacuum effects associated with the ALD processes (see Figure S4, Supporting Information) and so attribute the modified PL to the existence of the dielectric film. The spectral reshaping and downshift in PL energy seen here following deposition of Al_2O_3 and HfO_2 suggests both films *n*-type dope 1L MoS_2.[30,37] Such a doping effect has been attributed to a charge transfer between MoS_2 and trap states at the dielectric/MoS_2 interface.[23,60–62] The attenuated, redshifted, and widened MoS_2 PL spectrum observed after direct ALD of an Al_2O_3 layer is in excellent agreement with previous reports.[23,30] The effects of HfO_2-encapsulation on the PL behavior of 1L MoS_2 are less well-established. An enhanced and blueshifted PL emission following thermal ALD of HfO_2 was reported by Price et al., yet this is clearly inconsistent with our observations.[63] There, the authors concluded that dielectric screening effects, rather than charge doping, dominated the PL character of the HfO_2/MoS_2 structure. On the other hand, both Kim et al. and Yan et al. have observed a redshifted PL

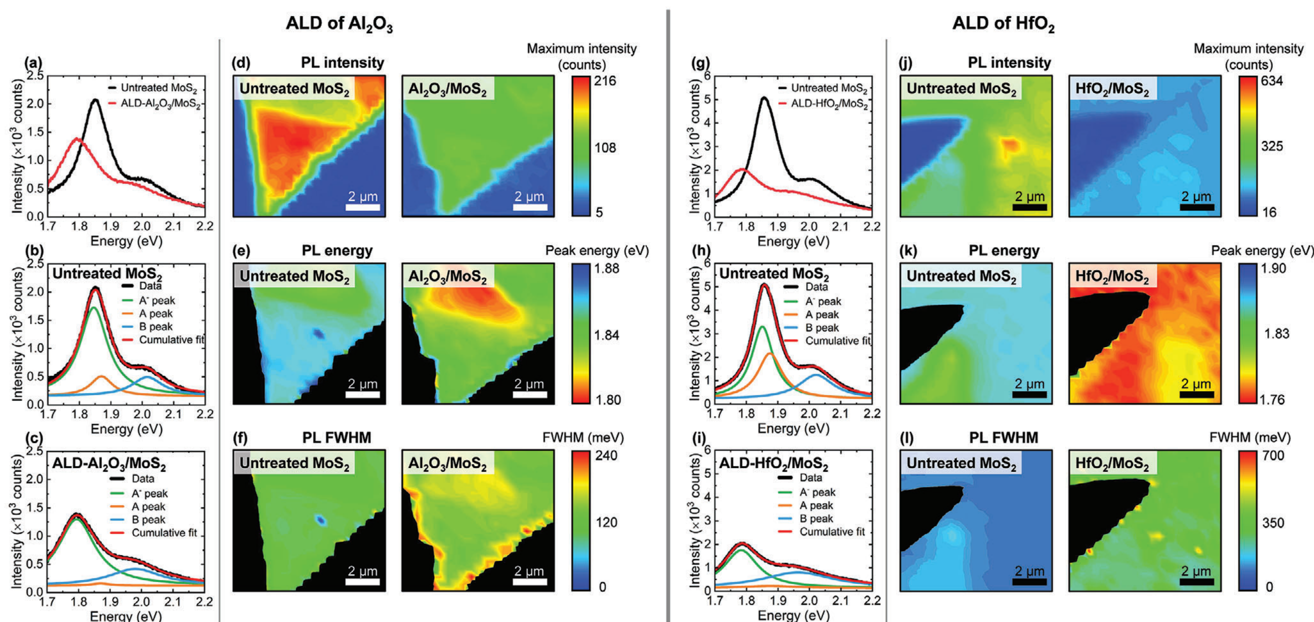

Figure 4. Raw single-spot PL spectra, multipeak deconvolution of the PL spectra from each MoS_2 sample before and after thermal ALD of (a–d) Al_2O_3 and (g–i) HfO_2. The cumulative fit, and contributions of the A_b, A^-, A and B peaks are given in red, pink, green, orange, and blue, respectively. Maps of the maximum absolute PL intensity, peak PL energy and FWHM of the PL signal emitted from each MoS_2 sample before and after ALD of (d–f) Al_2O_3 and (j–l) HfO_2.

© 2024 The Author(s). Advanced Materials Interfaces published by Wiley-VCH GmbH

21967350, 2024, 28, Downloaded from https://onlinelibrary.wiley.com/doi/10.1002/admi.202400305 by Test, Wiley Online Library on [03/10/2024]. See the Terms and Conditions (https://onlinelibrary.wiley.com/terms-and-conditions) on Wiley Online Library for rules of use; OA articles are governed by the applicable Creative Commons License

21967350, 2024, 28, Downloaded from https://onlinelibrary.wiley.com/doi/10.1002/admi.202400305 by Test, Wiley Online Library on [03/10/2024]. See the Terms and Conditions (https://onlinelibrary.wiley.com/terms-and-conditions) on Wiley Online Library for rules of use; OA articles are governed by the applicable Creative Commons License

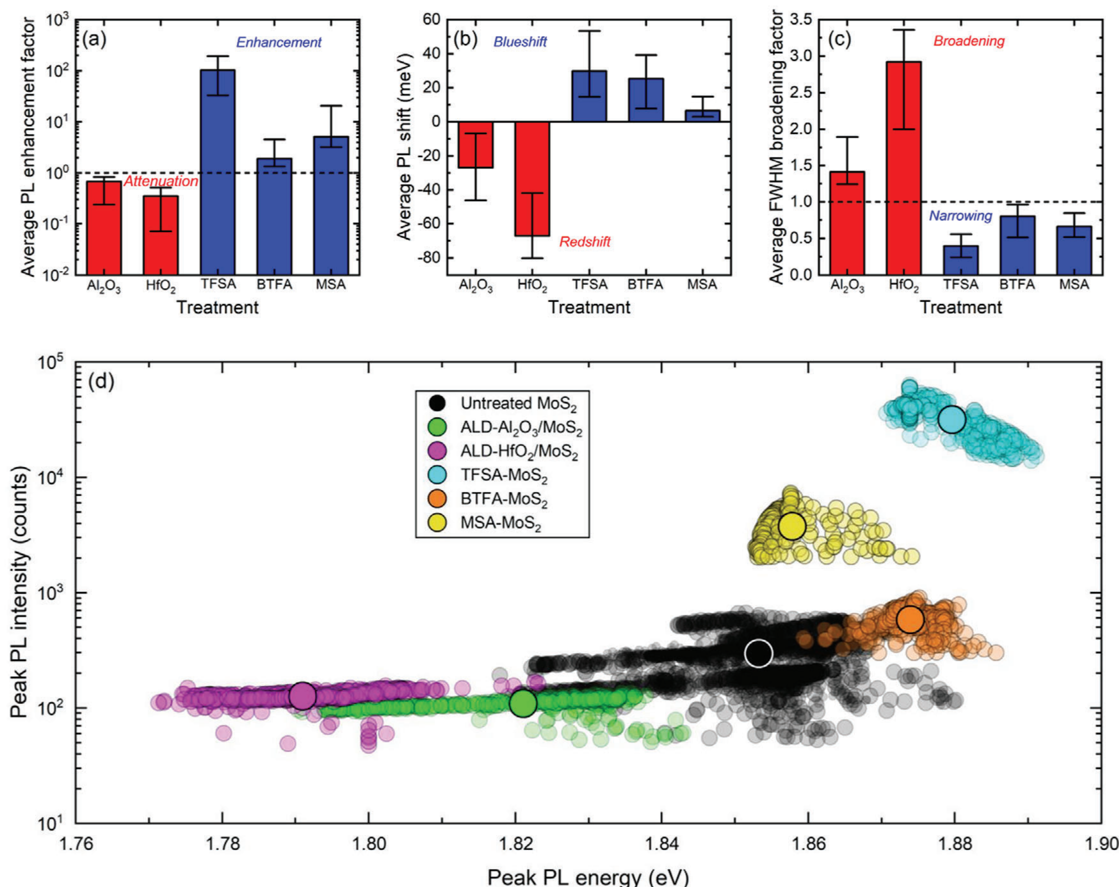

Figure 5. Comparison of average a) PL enhancement factors, b) shifts in PL energy, and c) PL FWHM broadening factors. The scatter bars indicate the range associated with each value. d) Peak PL intensity as a function of the corresponding peak PL energy for each applied treatment. The small translucent markers arise from every pixel extracted from each relevant PL map, with the larger solid circles indicating each calculated mean. The logarithmic scale to account for the large increase in PL intensity following TFSA treatment should be noted in (a) and (d).

spectrum from ALD-HfO_2/MoS_2 that is explained by an *n*-doping effect, in good agreement with our PL data.[23,64] The attenuation of absolute PL intensity following ALD of either Al_2O_3 or HfO_2 can be ascribed to a combination of *n*-type doping and the introduction of additional defect states.[65] Compared to the effects of Al_2O_3, we find ALD of HfO_2 yields a greater reduction in the 1L MoS_2 PL intensity. Moreover, the PL energy is downshifted more significantly (by ≈70 meV) following ALD of HfO_2, with a larger increase in FWHM also observed. The more pronounced alteration of the PL spectrum of 1L MoS_2 seen here following ALD of HfO_2 may indicate a stronger *n*-type doping effect at the dielectric/MoS_2 interface.

Changes to the A^-/A intensity ratio in 1L MoS_2 following each ALD process may reveal any doping effects. We deconvolute the single-spot MoS_2 PL spectra before and after deposition of each dielectric into constituent excitonic and trionic contributions. The decomposed PL data associated with the ALD of Al_2O_3 are shown in Figure 4b,c, with the multipeak fitting of the PL spectra before and after ALD of HfO_2 presented in Figure 4h,i. We find that both ALD processes explored in this study yield a significantly increased trion contribution, consistent with an *n*-type doping effect. The A^-/A ratio was seen to increase from ≈3.4 to ≈8.1 after Al_2O_3 growth and from ≈1.5 to ≈7.6 following deposition of HfO_2. We conclude that charge transfer at the dielectric/MoS_2 interface dominates the modified PL emission observed here following ALD of the high-κ Al_2O_3 and HfO_2 films.

2.3. Comparison of PL for Chemical Treatment and ALD-Dielectric Growth

We next comparatively assess the effects on the optical properties of 1L MoS_2 of the TFSA, BTFA, and MSA chemical treatments and the ALD growth of Al_2O_3 and HfO_2. We define a PL enhancement factor as the ratio of maximum absolute PL intensity averaged from PL mapping data after treatment to that obtained from the corresponding untreated MoS_2 sample. We also introduce an analogous FWHM broadening factor to evaluate any alteration of the PL spectral width. **Figure 5** presents a comparison of the average enhancement factors, shifts and broadening factors associated with each treatment investigated in this study, as extracted from PL maps. To allow intuitive visualization of changes in PL intensity and energy induced by each treatment, we plot the maximum PL intensity against the corresponding PL energy in Figure 5d.

© 2024 The Author(s). Advanced Materials Interfaces published by Wiley-VCH GmbH

Figure 5 shows that treating 1L MoS_2 with TFSA, BTFA or MSA gives rise to an enhanced, blueshifted, and sharpened PL emission. ALD of Al_2O_3 or HfO_2 on 1L MoS_2 induces opposing changes to the PL spectrum, yielding an attenuated, redshifted, and broadened signal. The PL character of 1L MoS_2 can therefore be selectively controlled via either chemical treatment or ALD of a high-κ material. The PL intensity can be tuned across two orders of magnitude, with TFSA treatment giving rise to a PL enhancement of up to ≈100× and ALD of a HfO_2 film reducing the signal strength by a factor of ≈3. Selecting the applied external treatment also enables a bidirectional shift in PL energy over a wide ≈200 meV spectral range. Moreover, the PL FWHM can be modulated by a factor of ≈0.4× up to ≈3×. The varying modifications to the MoS_2 PL signal that arise from each individual treatment are likely to result from charge doping effects.

2.4. Analysis of Doping and Strain by Raman Spectroscopy

We further examine extrinsic doping of 1L MoS_2 via spatially resolved Raman spectroscopy. The distinct Raman signature of 1L MoS_2 comprises two characteristic modes (an in-plane $E^1{}_{2g}$ vibration at ≈384 cm^{-1} and an out-of-plane $A^1{}_g$ feature at ≈403 cm^{-1})[66] that are known to be particularly responsive to charge doping and strain effects.[67] Single-spot Raman spectra were obtained from each 1L MoS_2 sample before and after each treatment and are displayed in **Figure 6**, with maps of the characteristic MoS_2 Raman peak positions and their separation provided in Figures S5–S9 (Supporting Information). We quantitatively evaluate the treatment-induced changes in the biaxial mechanical strain, ϵ, and electron density, n, of 1L MoS_2 by employing a process previously described by other authors for graphene[68–72] and more recently MoS_2.[31,32,73–75] For each treatment, we construct a correlative plot of $A^1{}_g$ versus $E^1{}_{2g}$ Raman peak positions extracted from Raman mapping data and overlay a ϵ-n coordinate system, and these plots are displayed in Figure 6. As detailed in Section S6 (Supporting Information), the dashed black lines represent strain isolines and correspond to $\Delta\epsilon = \pm 0.1\%$ variations in the strain. $\Delta\epsilon > 0$ indicates tensile strain, whereas $\Delta\epsilon < 0$ signifies compressive strain. Red dashes outline the doping isolines and indicate relative changes in the electron density of $\Delta n = \pm 0.1 \times 10^{13}$ cm^{-2}, where n-type doping is represented by $\Delta n > 0$ and p-type doping is implied by $\Delta n < 0$. The strain-free and undoped isolines intersect at a point that corresponds to literature values of Raman peak positions for a suspended CVD-synthesized 1L MoS_2 ($E^1{}_{2g}$ ≈385 cm^{-1} and $A^1{}_g$ ≈405 cm^{-1}) and this is outlined in Figure S10 (Supporting Information).[75,76]

A blueshift in the position of the out-of-plane $A^1{}_g$ Raman mode (≈0.9 cm^{-1} on average) was induced following TFSA immersion. The in-plane $E^1{}_{2g}$ peak experienced a comparatively smaller redshift of ≈0.3 cm^{-1}, thus yielding an overall increase in the peak separation across the 1L MoS_2. These observations are consistent with the widely reported Raman spectrum of p-doped 1L MoS_2,[77–80] with the $E^1{}_{2g}$ vibration known to be largely insensitive to electron doping due to its relatively weak electron-phonon coupling.[81] The correlative plot of the $A^1{}_g$ versus $E^1{}_{2g}$ peak positions confirms the p-type doping of the TFSA-treated 1L MoS_2 sample, and we estimate the electron density to be reduced by ≈0.5 × 10^{13} cm^{-2}, consistent with recent studies.[53,82] We find the characteristic MoS_2 Raman modes are both blueshifted by ≈0.5 cm^{-1} after BTFA treatment, with the Raman peak separation therefore relatively unchanged. Submersion in MSA, however, yields a very similar upward shift in the position of the $A^1{}_g$ peak (≈0.9 cm^1) to that seen following TFSA treatment, but here the $E^1{}_{2g}$ vibration is blueshifted by ≈0.4 cm^{-1}. Compared to TFSA and MSA treatment, a greater shift in the position of the in-plane $E^1{}_{2g}$ Raman mode was seen after BTFA submersion but the blueshift in the average $A^1{}_g$ peak position is less significant. From correlative plots of $A^1{}_g$ versus $E^1{}_{2g}$ peak positions, we infer that BTFA and MSA treatment both p-dope MoS_2, in excellent agreement with our PL analysis. We deduce that MSA treatments result in stronger p-type doping, reducing the MoS_2 electron density by ≈0.4 × 10^{13} cm^{-2}, compared to the ≈0.1 × 10^{13} cm^{-2} reduction estimated following BTFA submersion. This indicates that BTFA induces a weaker p-type doping effect than TFSA or MSA treatment.

ALD of Al_2O_3 was seen to yield a clear redshift of the $A^1{}_g$ peak (≈0.7 cm^{-1}) and a smaller redshift in the position of the $E^1{}_{2g}$ vibration (≈0.4 cm^{-1}), further evidencing n-type doping of MoS_2.[81] An n-doping is also observed following ALD of HfO_2, with a sizeable redshift in the $A^1{}_g$ Raman mode (≈3.1 cm^{-1}) position and a much smaller accompanying redshift of the $E^1{}_{2g}$ vibration (≈0.1 cm^{-1}). Substantial softening of the $A^1{}_g$ peak following thermal ALD of HfO_2 on 1L MoS_2 has been reported by Yan et al., in agreement with our PL data, which suggests much stronger doping occurs from HfO_2 growth compared to Al_2O_3.[64] It has been postulated that greater doping by HfO_2 is due to a higher density of charged defects at the HfO_2/MoS_2 interface, as the bulky TDMAH precursor renders initial HfO_2 nucleation on 1L MoS_2 slower than that of Al_2O_3.[32]

Raman spectral analysis of the treatments studied here confirms the charge doping effects indicated by the PL spectra. The polarity of the induced doping effect has a clear dependence on the choice of applied treatment. An n-type doping of 1L MoS_2 was observed following ALD of Al_2O_3 or HfO_2 films, whereas MoS_2 was found to be p-doped by TFSA, BTFA or MSA treatment. We postulate that the depletion of electron density in the chemically treated MoS_2 samples arises from the presence of electronegative F atoms, significant S vacancy passivation, or a combination of these two effects. Conversely, charge transfer at the dielectric/MoS_2 interface appears to increase the carrier density in 1L MoS_2.

The correlative plots also indicate treatment-induced changes in the strain of 1L MoS_2. All treatments investigated in this study, except TFSA submersion, were found to compressively strain 1L MoS_2. TFSA treatment was seen to introduce tensile strain ($\Delta\epsilon$ ≈−0.1%). This result contradicts previous reports that have claimed, by evaluation of single-site Raman spectra, that the strain in 1L MoS_2 is unchanged by submersion in TFSA.[27,83] However, our estimated ≈0.1% increase in tensile strain after superacid treatment agrees well with more recent reports that utilize a Raman mapping approach.[40,53,82] The origin of the increased tension in TFSA-treated 1L MoS_2 is not fully understood but it has been reported to result from direct repair of S vacancies. The removal of S vacancy sites yields an increase in the in-plane lattice parameters of 1L MoS_2, thus introducing biaxial tensile strain.[40,53] While TFSA was seen to increase the tension in 1L MoS_2, we find that BTFA treatment introduces compressive

© 2024 The Author(s). Advanced Materials Interfaces published by Wiley-VCH GmbH

21967350, 2024, 28, Downloaded from https://onlinelibrary.wiley.com/doi/10.1002/admi.202400305 by Test, Wiley Online Library on [03/10/2024]. See the Terms and Conditions (https://onlinelibrary.wiley.com/terms-and-conditions) on Wiley Online Library for rules of use; OA articles are governed by the applicable Creative Commons License

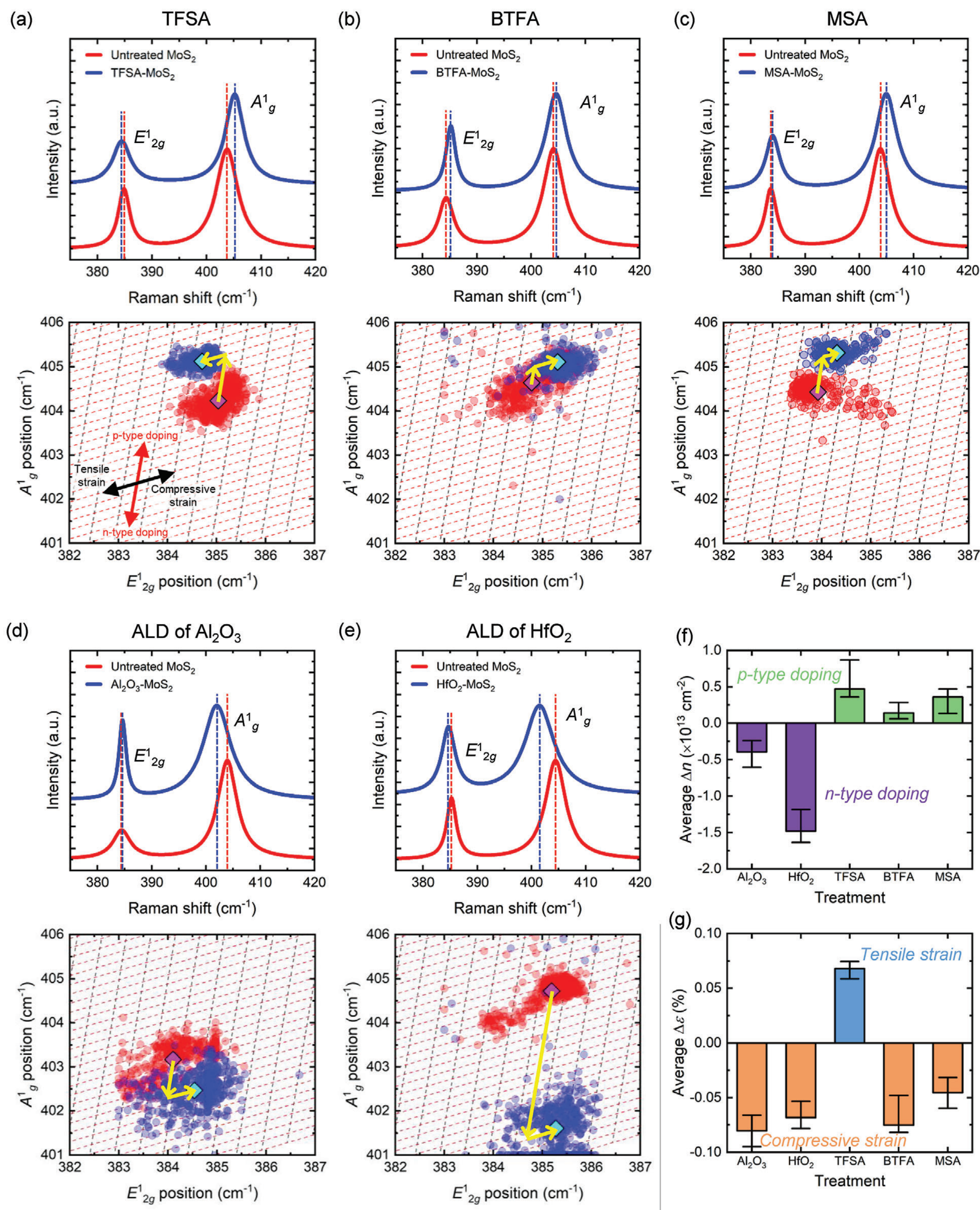

Figure 6. Single-spot Raman spectra and correlative plots of $A^1{}_g$ and $E^1{}_{2g}$ peak positions extracted from Raman mapping data for each chemical and ALD treatment: a) TFSA, b) BTFA, c) MSA, d) ALD of Al_2O_3, and e) ALD of HfO_2. The small circular translucent markers arise from every pixel extracted from the Raman mapping data and the large diamond points indicate the corresponding average values. Strain isolines (black dashed lines) correspond to $\Delta\epsilon = \pm 0.1\%$ variations in the strain and doping isolines (red dashed lines) indicate relative changes in the electron density of $\Delta n = \pm 0.1 \times 10^{13}$ cm^{-2}. The directions of the strain and doping effects are highlighted. Comparison of the average relative changes in f) electron density, Δn, and g) mechanical biaxial strain, $\Delta\epsilon$, for each applied treatment. The scatter bars indicate the range associated with each average value.

 © 2024 The Author(s). Advanced Materials Interfaces published by Wiley-VCH GmbH

21967350, 2024, 28, Downloaded from https://onlinelibrary.wiley.com/doi/10.1002/admi.202400305 by Test, Wiley Online Library on [03/10/2024]. See the Terms and Conditions (https://onlinelibrary.wiley.com/terms-and-conditions) on Wiley Online Library for rules of use; OA articles are governed by the applicable Creative Commons License

ADVANCED MATERIALS INTERFACES
Open Access
www.advmatinterfaces.de

strain ($\Delta\epsilon \approx 0.1\%$). Since increased tensile strain is associated with the repair of S vacancies,[40] we infer that significant defect passivation does not occur during BTFA submersion due to its S-free nature, consistent with our evaluation of the B/(A+A$^-$) ratio. MSA does, however, possess sulfonyl functionality so the absence of increased tensile strain in the MSA-treated 1L MoS_2 sample, while somewhat surprising, perhaps may result from residual solvent on the monolayer surface.[84] ALD of atop dielectric films has been reported to impart tensile strain on 1L MoS_2.[32,64,85] We speculate that the compressive strain induced by the high-κ films in this work originates from introduction of defect states during the growth process, since complete coalescence of the dielectric islands was not achieved even after 200 ALD cycles. Further work is required to fully understand the strain effects in 1L MoS_2 following chemical treatment and direct ALD of dielectrics.

3. Conclusion

Our systematic investigation has shown that varying degrees of enhancement, blueshift and narrowing of the PL emission from 1L MoS_2 result from submersion in TFSA, BTFA, or MSA solution due to *p*-type doping effects. Conversely, direct thermal ALD of a relatively thick atop Al_2O_3 or HfO_2 film was found to *n*-type dope 1L MoS_2, thus attenuating, redshifting, and broadening the PL signal. Control of the optical properties of monolayer TMDCs is important for future atomically thin optoelectronic devices and we have demonstrated facile tunability of the PL behavior of 1L MoS_2 via selective application of chemical treatment or dielectric growth.

4. Experimental Section

Chemicals and Materials: Bis(trifluoromethane)sulfonamide (TFSA, ≥95.0%), bis(trifluoroacetamide) (BTFA) and methanesulfonamide (MSA, ≥98%) were obtained from Sigma–Aldrich, with dichloromethane (DCM, 99.7+%) acquired from Alfa-Aesar. Two 1 cm × 1 cm 1L MoS_2 films (>99%) grown on SiO_2/Si via atomic pressure chemical vapor deposition (APCVD) were supplied by 2D Semiconductors[86] and each cleaved into at least nine smaller samples of approximately equal size. The films were supplied in vacuum-sealed packaging and cleaved samples were stored in a desiccator to alleviate any degradation effects due to ambient exposure.[87]

Chemical Treatment: TFSA, BTFA, and MSA were dissolved in anhydrous DCM at a concentration of 2 mg mL^{-1}. A high-specification filtered and sealed MBRAUN UNIlab modular glovebox with gas purification system, solvent filter, and controlled low-humidity atmosphere (<0.1 ppm of O_2 and H_2O) was used for the handling of TFSA and BTFA. MSA was handled in a lower specification glovebox with ambient flowing nitrogen (relative humidity <25%), and all solutions were prepared in this glovebox. The MoS_2 samples were immersed separately in the TFSA-DCM, BTFA-DCM, and MSA-DCM solutions for 10 min at room temperature before being removed and allowed to dry.

High-κ Dielectric Deposition: Thermal ALD growth of Al_2O_3 and HfO_2 was performed at 200 °C using a Veeco Fiji G2 system. All depositions comprised 200 ALD cycles with water (H_2O) used as the co-reactant in each case and argon employed as the carrier and purging gas. Al_2O_3 was grown by pulsing trimethylaluminum (TMA) precursor for 0.06 s, and H_2O for 0.06 s, purging for 8 s between each step. To deposit HfO_2 films, tetrakis(dimethylamido)hafnium (TDMAH) precursor, heated to 75 °C, was pulsed for 0.25 s, followed by 0.06 s of H_2O, with an 8 s purge step before and after each.

Raman and PL Spectroscopy: Raman and PL data were acquired at room temperature using a Renishaw inVia Reflex Raman microscope in standard confocal mode with a 532 nm excitation laser at 0.1% of maximum power (≈0.18 µW). A 50× Leica objective lens was used, with a numerical aperture of 0.75 and a grating with 1800 lines mm^{-1}. Optical micrographs of the samples were acquired with this optical configuration. Single-spot Raman data were the sum of 4 accumulations of 5 s each, with the corresponding PL data the sum of 4 accumulations of 10 s each. Multipeak Lorentzian fitting of single-spot PL spectra was performed, with the exciton and trion peak energies constrained within approximate initial estimates and their linewidths allowed to vary freely. Raman and PL mapping data were also obtained for each sample, collected over an area of 12 µm × 12 µm with a step size of 0.5 µm. Each PL map was centered ≈1.85 eV and the spectrum at each point fitted with a single Lorentzian curve, with peak intensity extracted and mapped as a function of position. Similarly, a superposition of two Lorentzian functions was fitted to each Raman spectrum to encompass the two characteristic MoS_2 peaks. The exposure conditions used to acquire PL/Raman spectra following an applied treatment were identical to those used to measure the corresponding untreated MoS_2. All data were recorded via the Renishaw WiRE 3.1 software package and cosmic-ray features were eliminated where necessary.

Atomic Force Microscopy: Surface topographies were imaged via atomic force microscopy (AFM) using a Bruker Dimension Icon in the PeakForce Tapping Mode and a ScanAsystAir tip (with a nominal tip length of 115 µm, a tip radius of 2 nm and a spring constant of 0.4 Nm^{-1}).[88] All AFM images were taken with 256 lines per scan at a scan rate of 0.5 Hz to yield an appropriate resolution. The Gwyddion 2.60 software package was used for image processing and analysis.[89] The surface coverage of the ALD-dielectric films was estimated using the Fiji distribution of the ImageJ software package, by converting the AFM maps to 8-bit grayscale and subsequently binary images via the software's thresholding algorithm.[90]

Statistical Analysis: Statistical analysis was performed on the PL mapping data presented in Figures 1,2, and 4 in the main text and on the Raman maps provided in Figures S5–S9 (Supporting Information). The Raman and PL maps were obtained over a 12 µm × 12 µm area (144 µm^2) with a step size of 0.5 µm to yield 625 data points per map. The mean average PL enhancement factors, PL shifts, PL broadening factors, doping, and strain values were then calculated from the PL and Raman mapping distributions. Origin2021b software by OriginLab Corporation, combined with MATLAB code written by the authors and executed in MATLAB R2021b by MathWorks, was used for this statistical analysis.

Supporting Information

Supporting Information is available from the Wiley Online Library or from the author.

Acknowledgements

The authors acknowledge the use of the Raman/PL facilities within the Spectroscopy Research Technology Platform (RTP), University of Warwick, and the AFM facilities within the Electron Microscopy RTP, University of Warwick, which are part of the Warwick Analytical Science Centre supported by EPSRC (EP/V007688/1).

Conflict of Interest

The authors declare no conflict of interest.

Data Availability Statement

The data that support the findings of this study are openly available in Warwick Research Archive Portal (WRAP) at https://wrap.warwick.ac.uk/186839.

© 2024 The Author(s). Advanced Materials Interfaces published by Wiley-VCH GmbH

21967350, 2024, 28, Downloaded from https://onlinelibrary.wiley.com/doi/10.1002/admi.202400305 by Test, Wiley Online Library on [03/10/2024]. See the Terms and Conditions (https://onlinelibrary.wiley.com/terms-and-conditions) on Wiley Online Library for rules of use; OA articles are governed by the applicable Creative Commons License

Keywords

ALD, doping, high-κ dielectrics, high-$\kappa\kappa$ dielectrics, monolayer MoS_2, photoluminescence, superacid, transition metal dichalcogenides

Received: April 10, 2024
Revised: June 19, 2024
Published online: July 10, 2024

[1] X. Duan, C. Wang, A. Pan, R. Yu, X. Duan, *Chem. Soc. Rev.* **2015**, *44*, 8859.
[2] W. Choi, N. Choudhary, G. H. Han, J. Park, D. Akinwande, Y. H. Lee, *Mater. Today* **2017**, *20*, 116.
[3] B. Radisavljevic, A. Radenovic, J. Brivio, V. Giacometti, A. Kis, *Nat. Nanotechnol.* **2011**, *6*, 147.
[4] O. Lopez-Sanchez, D. Lembke, M. Kayci, A. Radenovic, A. Kis, *Nat. Nanotechnol.* **2013**, *8*, 497.
[5] M. Nayeri, M. Moradinasab, M. Fathipour, *Semicond. Sci. Technol.* **2018**, *33*, 025002.
[6] M. G. Burdanova, M. Liu, M. Staniforth, Y. Zheng, R. Xiang, S. Chiashi, A. Anisimov, E. I. Kauppinen, S. Maruyama, J. Lloyd-Hughes, *Adv. Funct. Mater.* **2022**, *32*, 2104969.
[7] I. Zeimpekis, T. Rahman, O. M. Leung, J. Tyson, M. Ebert, S. A. Boden, C. Ponce De Leon, K. A. Morgan, *ACS Appl. Energy Mater.* **2024**, *7*, 2299.
[8] M. Chhowalla, H. S. Shin, G. Eda, L.-J. Li, K. P. Loh, H. Zhang, *Nat. Chem.* **2013**, *5*, 263.
[9] A. Splendiani, L. Sun, Y. Zhang, T. Li, J. Kim, C.-Y. Chim, G. Galli, F. Wang, *Nano Lett.* **2010**, *10*, 1271.
[10] J. Jeon, S. K. Jang, S. M. Jeon, G. Yoo, Y. H. Jang, J.-H. Park, S. Lee, *Nanoscale* **2015**, *7*, 1688.
[11] N. Thomas, S. Mathew, K. M. Nair, K. O'Dowd, P. Forouzandeh, A. Goswami, G. McGranaghan, S. C. Pillai, *Mater. Today Sustainability* **2021**, *13*, 100073.
[12] O. K. Le, V. Chihaia, V. Van On, D. N. Son, *RSC Adv.* **2021**, *11*, 8033.
[13] N. Kang, H. P. Paudel, M. N. Leuenberger, L. Tetard, S. I. Khondaker, *J. Phys. Chem. C* **2014**, *118*, 21258.
[14] H. Nan, Z. Wang, W. Wang, Z. Liang, Y. Lu, Q. Chen, D. He, P. Tan, F. Miao, X. Wang, J. Wang, Z. Ni, *ACS Nano* **2014**, *8*, 1231.
[15] X. Wei, Z. Yu, F. Hu, Y. Cheng, L. Yu, X. Wang, M. Xiao, J. Wang, X. Wang, Y. Shi, *AIP Adv.* **2014**, *4*, 123004.
[16] H.-J. Kim, Y. J. Yun, S. N. Yi, S. K. Chang, D. H. Ha, *ACS Omega* **2020**, *5*, 7903.
[17] S. Golovynskyi, O. I. Datsenko, D. Dong, Y. Lin, I. Irfan, B. Li, D. Lin, J. Qu, *J. Phys. Chem. C* **2021**, *125*, 17806.
[18] R. Peng, X. Ma, Z. D. Hood, A. Boulesbaa, A. A. Puretzky, J. Tong, Z. Wu, *J. Mater. Chem. A* **2023**, *11*, 16714.
[19] A. Kaushik, J. Singh, R. Soni, J. P. Singh, *ACS Appl. Nano Mater.* **2023**, *6*, 9236.
[20] I. Irfan, S. Golovynskyi, O. A. Yeshchenko, M. Bosi, T. Zhou, B. Xue, B. Li, J. Qu, L. Seravalli, *Phys. E* **2022**, *140*, 115213.
[21] Z.-M. Wang, C.-B. Yao, L.-Y. Wang, X. Wang, C.-H. Jiang, H.-T. Yin, *ACS Appl. Mater. Interfaces* **2023**, *15*, 17364.
[22] S. L. Pain, N. E. Grant, J. D. Murphy, *ACS Nano* **2022**, *16*, 1260.
[23] S. Y. Kim, H. I. Yang, W. Choi, *Appl. Phys. Lett.* **2018**, *113*, 133104.
[24] B. F. M. Healy, S. L. Pain, J. Lloyd-Hughes, N. E. Grant, J. D. Murphy, *Mater. Res. Express* **2024**, *11*, 015002.
[25] Z. Liu, M. Amani, S. Najmaei, Q. Xu, X. Zou, W. Zhou, T. Yu, C. Qiu, A. G. Birdwell, F. J. Crowne, R. Vajtai, B. I. Yakobson, Z. Xia, M. Dubey, P. M. Ajayan, J. Lou, *Nat. Commun.* **2014**, *5*, 5246.
[26] L. Tao, K. Chen, Z. Chen, W. Chen, X. Gui, H. Chen, X. Li, J.-B. Xu, *ACS Appl. Mater. Interfaces* **2017**, *9*, 12073.
[27] M. Amani, D.-H. Lien, D. Kiriya, J. Xiao, A. Azcatl, J. Noh, S. R. Madhvapathy, R. Addou, S. Kc, M. Dubey, K. Cho, R. M. Wallace, S.-C. Lee, J.-H. He, J. W. Ager, X. Zhang, E. Yablonovitch, A. Javey, *Science* **2015**, *350*, 1065.
[28] M. Amani, P. Taheri, R. Addou, G. H. Ahn, D. Kiriya, D.-H. Lien, J. W. Ager III, R. M. Wallace, A. Javey, *Nano Lett.* **2016**, *16*, 2786.
[29] G. Plechinger, F. X. Schrettenbrunner, J. Eroms, D. Weiss, C. Schüller, T. Korn, *Phys. Status Solidi RRL* **2012**, *6*, 126.
[30] Y. Li, X. Li, H. Chen, J. Shi, Q. Shang, S. Zhang, X. Qiu, Z. Liu, Q. Zhang, H. Xu, W. Liu, X. Liu, Y. Liu, *ACS Appl. Mater. Interfaces* **2017**, *9*, 27402.
[31] E. Schilirò, R. L. Nigro, S. E. Panasci, S. Agnello, M. Cannas, F. M. Gelardi, F. Roccaforte, F. Giannazzo, *Adv. Mater. Interfaces* **2021**, *8*, 2101117.
[32] E. Schilirò, S. E. Panasci, A. M. Mio, G. Nicotra, S. Agnello, B. Pecz, G. Z. Radnoczi, I. Deretzis, A. La Magna, F. Roccaforte, R. Lo Nigro, F. Giannazzo, *Appl. Surf. Sci.* **2023**, *630*, 157476.
[33] F. Carrascoso, R. Frisenda, A. Castellanos-Gomez, *Nano Mater. Sci.* **2022**, *4*, 44.
[34] R. Frisenda, A. Castellanos-Gomez, *Nat. Photonics* **2020**, *14*, 269.
[35] O. I. Datsenko, S. Golovynskyi, A. I. Pérez-Jiménez, M. Chaigneau, A. Golovynskyi, I. Golovynska, V. Shevchenko, M. Bosi, L. Seravalli, *Phys. E* **2023**, *154*, 115812.
[36] Y. Lin, X. Ling, L. Yu, S. Huang, A. L. Hsu, Y.-H. Lee, J. Kong, M. S. Dresselhaus, T. Palacios, *Nano Lett.* **2014**, *14*, 5569.
[37] S. Mouri, Y. Miyauchi, K. Matsuda, *Nano Lett.* **2013**, *13*, 5944.
[38] D.-H. Lien, S. Z. Uddin, M. Yeh, M. Amani, H. Kim, J. W. Ager, E. Yablonovitch, A. Javey, *Science* **2019**, *364*, 468.
[39] M. Amani, R. A. Burke, X. Ji, P. Zhao, D.-H. Lien, P. Taheri, G. H. Ahn, D. Kirya, J. W. Ager III, E. Yablonovitch, J. Kong, M. Dubey, A. Javey, *ACS Nano* **2016**, *10*, 6535.
[40] S. Roy, W. Choi, S. Jeon, D.-H. Kim, H. Kim, S. J. Yun, Y. Lee, J. Lee, Y.-M. Kim, J. Kim, *Nano Lett.* **2018**, *18*, 4523.
[41] K. F. Mak, K. He, C. Lee, G. H. Lee, J. Hone, T. F. Heinz, J. Shan, *Nat. Mater.* **2013**, *12*, 207.
[42] J. Suh, T.-E. Park, D.-Y. Lin, D. Fu, J. Park, H. J. Jung, Y. Chen, C. Ko, C. Jang, Y. Sun, R. Sinclair, J. Chang, S. Tongay, J. Wu, *Nano Lett.* **2014**, *14*, 6976.
[43] D. Vaquero, V. Clericò, J. Salvador-Sánchez, A. Martín-Ramos, E. Díaz, F. Domínguez-Adame, Y. M. Meziani, E. Diez, J. Quereda, *Commun. Phys.* **2020**, *3*, 194.
[44] H. Wang, C. Zhang, F. Rana, *Nano Lett.* **2015**, *15*, 339.
[45] K. M. McCreary, A. T. Hanbicki, S. V. Sivaram, B. T. Jonker, *APL Mater.* **2018**, *6*, 111106.
[46] Y. Kim, Y. Lee, H. Kim, S. Roy, J. Kim, *Nanoscale* **2018**, *10*, 8851.
[47] X. Dai, X. Zhang, I. M. Kislyakov, L. Wang, J. Huang, S. Zhang, N. Dong, J. Wang, *Opt. Express* **2019**, *27*, 13744.
[48] A. M. Z. Tan, C. Freysoldt, R. G. Hennig, *Phys. Rev. Mater.* **2020**, *4*, 064004.
[49] J. Hong, Z. Hu, M. Probert, K. Li, D. Lv, X. Yang, L. Gu, N. Mao, Q. Feng, L. Xie, J. Zhang, D. Wu, Z. Zhang, C. Jin, W. Ji, X. Zhang, J. Yuan, Z. Zhang, *Nat. Commun.* **2015**, *6*, 6293.
[50] W. Zhou, X. Zou, S. Najmaei, Z. Liu, Y. Shi, J. Kong, J. Lou, P. M. Ajayan, B. I. Yakobson, J.-C. Idrobo, *Nano Lett.* **2013**, *13*, 2615.
[51] H.-P. Komsa, A. V. Krasheninnikov, *Phys. Rev. B* **2015**, *91*, 125304.
[52] Z. Lin, B. R. Carvalho, E. Kahn, R. Lv, R. Rao, H. Terrones, M. A. Pimenta, M. Terrones, *2D Mater.* **2016**, *3*, 022002.
[53] H. Kim, T. Lee, H. Ko, S. Kim, H. Rho, *Appl. Phys. Lett.* **2020**, *117*, 202104.
[54] Y. Zhu, J. Lim, Z. Zhang, Y. Wang, S. Sarkar, H. Ramsden, Y. Li, H. Yan, D. Phuyal, N. Gauriot, A. Rao, R. L. Z. Hoye, G. Eda, M. Chhowalla, *ACS Nano* **2023**, *17*, 13545.
[55] S. M. George, *Chem. Rev.* **2010**, *110*, 111.
[56] S. McDonnell, B. Brennan, A. Azcatl, N. Lu, H. Dong, C. Buie, J. Kim, C. L. Hinkle, M. J. Kim, R. M. Wallace, *ACS Nano* **2013**, *7*, 10354.

© 2024 The Author(s). Advanced Materials Interfaces published by Wiley-VCH GmbH

21967350, 2024, 28, Downloaded from https://onlinelibrary.wiley.com/doi/10.1002/admi.202400305 by Test, Wiley Online Library on [03/10/2024]. See the Terms and Conditions (https://onlinelibrary.wiley.com/terms-and-conditions) on Wiley Online Library for rules of use; OA articles are governed by the applicable Creative Commons License

[57] H. Zhang, D. Chiappe, J. Meersschaut, T. Conard, A. Franquet, T. Nuytten, M. Mannarino, I. Radu, W. Vandervorst, A. Delabie, *J. Chem. Phys.* **2016**, *146*, 052810.
[58] H. Liu, K. Xu, X. Zhang, P. D. Ye, *Appl. Phys. Lett.* **2012**, *100*, 152115.
[59] K. M. Price, K. E. Schauble, F. A. McGuire, D. B. Farmer, A. D. Franklin, *ACS Appl. Mater. Interfaces* **2017**, *9*, 23072.
[60] J. Na, M.-K. Joo, M. Shin, J. Huh, J.-S. Kim, M. Piao, J.-E. Jin, H.-K. Jang, H. J. Choi, J. H. Shim, G.-T. Kim, *Nanoscale* **2014**, *6*, 433.
[61] A. Henning, S. Levashov, C. Qian, T. Grünleitner, J. Primbs, J. J. Finley, I. D. Sharp, *Adv. Mater. Interfaces* **2023**, *10*, 2202429.
[62] C. J. McClellan, E. Yalon, K. K. H. Smithe, S. V. Suryavanshi, E. Pop, *ACS Nano* **2021**, *15*, 1587.
[63] K. M. Price, S. Najmaei, C. E. Ekuma, R. A. Burke, M. Dubey, A. D. Franklin, *ACS Appl. Nano Mater.* **2019**, *2*, 4085.
[64] R. Yan, S. Bertolazzi, J. Brivio, T. Fang, A. Konar, A. Birdwell, N. Nguyen, A. Kis, D. Jena, H. Xing, *arXiv preprint* **2012**, 12114136v2.
[65] M. Turunen, H. Fernandez, S.-T. Akkanen, H. Seppänen, Z. Sun, *2D Mater.* **2023**, *10*, 045018.
[66] X. Zhang, X.-F. Qiao, W. Shi, J.-B. Wu, D.-S. Jiang, P.-H. Tan, *Chem. Soc. Rev.* **2015**, *44*, 2757.
[67] H.-J. Kim, D. Kim, S. Jung, M.-H. Bae, Y. J. Yun, S. N. Yi, J.-S. Yu, J.-H. Kim, D. H. Ha, *J. Raman Spectrosc.* **2018**, *49*, 1938.
[68] T. M. G. Mohiuddin, A. Lombardo, R. R. Nair, A. Bonetti, G. Savini, R. Jalil, N. Bonini, D. M. Basko, C. Galiotis, N. Marzari, K. S. Novoselov, A. K. Geim, A. C. Ferrari, *Phys. Rev. B* **2009**, *79*, 205433.
[69] J. E. Lee, G. Ahn, J. Shim, Y. S. Lee, S. Ryu, *Nat. Commun.* **2012**, *3*, 1024.
[70] C. Androulidakis, G. Tsoukleri, N. Koutroumanis, G. Gkikas, P. Pappas, J. Parthenios, K. Papagelis, C. Galiotis, *Carbon* **2015**, *81*, 322.
[71] A. Armano, G. Buscarino, M. Cannas, F. M. Gelardi, F. Giannazzo, E. Schilirò, S. Agnello, *Carbon* **2018**, *127*, 270.
[72] E. Schilirò, R. Lo Nigro, S. E. Panasci, F. M. Gelardi, S. Agnello, R. Yakimova, F. Roccaforte, F. Giannazzo, *Carbon* **2020**, *169*, 172.
[73] A. Michail, N. Delikoukos, J. Parthenios, C. Galiotis, K. Papagelis, *Appl. Phys. Lett.* **2016**, *108*, 173102.
[74] W. H. Chae, J. D. Cain, E. D. Hanson, A. A. Murthy, V. P. Dravid, *Appl. Phys. Lett.* **2017**, *111*, 143106.
[75] S. E. Panasci, E. Schilirò, G. Greco, M. Cannas, F. M. Gelardi, S. Agnello, F. Roccaforte, F. Giannazzo, *ACS Appl. Mater. Interfaces* **2021**, *13*, 31248.
[76] D. Lloyd, X. Liu, J. W. Christopher, L. Cantley, A. Wadehra, B. L. Kim, B. B. Goldberg, A. K. Swan, J. S. Bunch, *Nano Lett.* **2016**, *16*, 5836.
[77] S. Tongay, J. Zhou, C. Ataca, J. Liu, J. S. Kang, T. S. Matthews, L. You, J. Li, J. C. Grossman, J. Wu, *Nano Lett.* **2013**, *13*, 2831.
[78] N. Mao, Y. Chen, D. Liu, J. Zhang, L. Xie, *Small* **2013**, *9*, 1312.
[79] B. Chakraborty, A. Bera, D. V. S. Muthu, S. Bhowmick, U. V. Waghmare, A. K. Sood, *Phys. Rev. B* **2012**, *85*, 161403.
[80] A. Rai, A. Valsaraj, H. C. Movva, A. Roy, R. Ghosh, S. Sonde, S. Kang, J. Chang, T. Trivedi, R. Dey, S. Guchhait, S. Larentis, L. F. Register, E. Tutuc, S. K. Banerjee, *Nano Lett.* **2015**, *15*, 4329.
[81] B. Miller, E. Parzinger, A. Vernickel, A. W. Holleitner, U. Wurstbauer, *Appl. Phys. Lett.* **2015**, *106*, 122103.
[82] T. Lee, Y.-G. Yoon, S. W. Lee, J.-H. Ahn, H. Rho, *Appl. Surf. Sci.* **2023**, *637*, 157885.
[83] A. Alharbi, P. Zahl, D. Shahrjerdi, *Appl. Phys. Lett.* **2017**, *110*, 033503.
[84] A. Jain, P. Bharadwaj, S. Heeg, M. Parzefall, T. Taniguchi, K. Watanabe, L. Novotny, *Nanotechnology* **2018**, *29*, 265203.
[85] W. S. Yun, S. W. Han, S. C. Hong, I. G. Kim, J. D. Lee, *Phys. Rev. B* **2012**, *85*, 033305.
[86] Y.-H. Lee, X.-Q. Zhang, W. Zhang, M.-T. Chang, C.-T. Lin, K.-D. Chang, Y.-C. Yu, J. T.-W. Wang, C.-S. Chang, L.-J. Li, T.-W. Lin, *Adv. Mater.* **2012**, *24*, 2320.
[87] J. Gao, B. Li, J. Tan, P. Chow, T.-M. Lu, N. Koratkar, *ACS Nano* **2016**, *10*, 2628.
[88] K. Xu, W. Sun, Y. Shao, F. Wei, X. Zhang, W. Wang, P. Li, *Nanotechnol. Rev.* **2018**, *7*, 605.
[89] D. Nečas, P. Klapetek, *Open Phys.* **2012**, *10*, 181.
[90] J. Schindelin, I. Arganda-Carreras, E. Frise, V. Kaynig, M. Longair, T. Pietzsch, S. Preibisch, C. Rueden, S. Saalfeld, B. Schmid, J.-Y. Tinevez, D. J. White, V. Hartenstein, K. Eliceiri, P. Tomancak, A. Cardona, *Nat. Methods* **2012**, *9*, 676.

© 2024 The Author(s). Advanced Materials Interfaces published by Wiley-VCH GmbH

21967350, 2024, 28, Downloaded from https://onlinelibrary.wiley.com/doi/10.1002/admi.202400305 by Test, Wiley Online Library on [03/10/2024]. See the Terms and Conditions (https://onlinelibrary.wiley.com/terms-and-conditions) on Wiley Online Library for rules of use; OA articles are governed by the applicable Creative Commons License